RSC Advances

PAPER

View Article Online
View Journal | View Issue

Cite this: *RSC Adv.*, 2026, **16**, 17351

Polydopamine enhances the photocatalytic performance of a BiOBr-loaded 3D-printed monolithic photoreactor by fused deposition modeling

Fengrui Wu,†[ad] Yan Li,†[ad] Wenxiu Wu,[bd] Zhipeng Zhang,[bd] Liangbin Lin,[bd] Songwei Yang,[bd] Lihong Xu,[c] Xinshu Xia,[bd] Weiming Zhou, *[bd] Changlin Cao *[bd] and Liren Xiao*[ad]

Further improvement in the performance of monolithic photoreactors is crucial for their practical applications. Herein, a BiOBr@PDA composite was prepared *via* the solvothermal method, and then, it was loaded onto a 3D-printed monolithic photoreactor under ambient conditions to form the 20D-BiOBr@PDA photocatalyst. Using rhodamine B (RhB) as a model pollutant, the photocatalytic activity of the prepared devices was systematically evaluated. Results revealed that tuning the amount of polydopamine (PDA) coating significantly influenced the photocatalytic performance. When 20 mL of a dopamine solution was employed, the resulting 20D-BiOBr@PDA exhibited the highest photocatalytic efficiency, achieving a 95.0% degradation of RhB within 1 h. Furthermore, selective degradation experiments were conducted using various pollutants, including cationic dyes (RhB and methylene blue (MB)), an anionic dye (methyl orange (MO)), and an antibiotic (tetracycline (TC)). The 20D-BiOBr@PDA photocatalyst demonstrated the most pronounced degradation toward RhB, while the degradation efficiencies for MB, MO, and TC reached 94.3%, 47.3%, and 55.0%, respectively, after 3 h. Reactive species trapping experiments identified superoxide radicals ($\cdot O^{2-}$) as the predominant reactive species responsible for RhB degradation. Moreover, cyclic stability tests indicated that after 10 continuous cycles, the degradation efficiency of 20D-BOB@PDA for RhB remained at 90.0% within 1 h, confirming its excellent reusability and stability. This new approach introduces conductive polymers to enhance the photocatalytic performance of monolithic photoreactors.

Received 13th February 2026
Accepted 16th March 2026

DOI: 10.1039/d6ra01291d

rsc.li/rsc-advances

Introduction

With the growing demand for environmental protection strategies and rapid advancements in clean energy conversion technologies, photocatalysis has emerged as a central research focus in materials chemistry and environmental engineering. Its intrinsic advantages, such as environmental friendliness, high efficiency, and broad applicability, make it particularly attractive for applications like the degradation of organic pollutants and photocatalytic water splitting for hydrogen generation.[1–3] However, traditional photocatalysts are typically composed of micron- or nano-scale powders, which tend to agglomerate during their use. This agglomeration not only reduces the effective photocatalytic surface area and reaction efficiency but also poses risks of secondary pollution.[4–6] To address these drawbacks, the development of monolithic photoreactors has been proposed as a promising solution. These reactors possess a honeycomb structure with internal channels on which photocatalysts are immobilized, thereby enhancing reactant-catalyst contact, facilitating catalyst recovery, and minimizing the risk of secondary pollution.[7–10]

Despite these advantages, the conventional manufacturing methods used for monolithic photoreactors, such as extrusion molding and compression sintering, have several drawbacks, including structural inhomogeneity, limited flexibility in designing complex geometries, and the uneven distribution of functional components.[11] All these factors limit the photocatalytic efficiency of monolithic photoreactors. In contrast, the fused deposition modeling (FDM) 3D printing technology offers a versatile and cost-effective alternative for constructing photocatalytic supports. This layer-by-layer additive manufacturing

[a]*College of Chemistry and Materials Science, Fujian Normal University, Fuzhou 350117, China. E-mail: xlr1966@fjnu.edu.cn*

[b]*College of Environmental and Resource Sciences, Fujian Normal University, Fuzhou 350117, China. E-mail: wmzhou@fjnu.edu.cn; caochlin3@fjnu.edu.cn*

[c]*College of Materials Science and Engineering, Fujian University of Technology, Fuzhou 350117, China*

[d]*Engineering Research Centre of Polymer Green Recycling of Ministry of Education, Fuzhou 350117, China*

† These authors contributed equally to this work.

process achieves precise structural control through the use of thermoplastic filaments, thereby addressing the key limitations of traditional support fabrication methods.[12,13] FDM 3D printing possesses three main advantages. First, it offers exceptional controllability: parameters such as nozzle temperature, layer thickness, infill density, and printing path can be precisely adjusted to tailor both macroscopic geometry and microscopic porosity.[14,15] Second, it exhibits broad material compatibility beyond conventional thermoplastics, such as polylactic acid (PLA) and acrylonitrile-butadiene-styrene (ABS), and accommodates flexible polymers (*e.g.*, polyethylene terephthalate glycol (PETG) and polyurethane (TPU)) and specialty composites, including wood-plastic and carbon fiber-reinforced materials.[12,16,17] Third, it provides high material utilization and fabrication efficiency, eliminating the need for complex molds and achieving nearly 100% material usage, thereby resolving the issues of uncontrollable morphology and uneven catalyst dispersion associated with traditional supports.[18]

Building upon the advantages of the FDM technology, integrating biological materials into 3D-printed supports has recently gained attention as a means to construct bio-material hybrid carriers that enhance photocatalytic performance. *Chlorella*, a unicellular green algal species, serves as an ideal photosensitizing component due to its abundance of chlorophyll a, chlorophyll b, and carotenoids, which confer a strong light-harvesting capability.[19] In our previous studies, *Chlorella* powder was pretreated *via* low-temperature drying and subsequently blended with PLA and poly(butylene adipate-*co*-terephthalate) (PBAT) to form PLA/PBAT/*Chlorella* composite materials. The results indicated that when the *Chlorella* loading was below 20 phr, the mechanical properties of the composite remained largely unaffected.[20] However, beyond this threshold, the mechanical strength and flexibility showed noticeable declines. Furthermore, a 3D printing filament containing 20 phr of *Chlorella* was fabricated, and it was printed into D-type models (Fig. S1). A BiOBr photocatalyst was subsequently immobilized on the surface of these models. The resulting system exhibited significantly improved cyclic stability compared with traditional granular carriers. However, the photocatalytic degradation efficiency of immobilized BiOBr for rhodamine B (RhB) remained notably lower than that of BiOBr powder (Fig. S2).

To further enhance the photocatalytic performance of the reactor by reducing the recombination of photogenerated carriers, polydopamine (PDA) has attracted considerable research interest due to its distinctive electronic and chemical properties. PDA, a polymerization product of dopamine (DA), contains functional groups, such as catechol, amine, and aromatic rings, and possesses an extended π-conjugated structure that enables efficient charge transport and strong absorption in the visible-light range.[21–23] Li *et al.* prepared Ti-PDA nanoparticles composed of bis(2-hydroxy propionic acid) diammonium titanium hydroxide (Ti-BALDH) chelated with dopamine, which exhibited excellent Cr(VI) adsorption and photoreduction performance under visible light, achieving a 99% reduction within 30 min and maintaining 95% efficiency after three cycles.[24] Similarly, Le *et al.* developed visible-light-responsive TiO_2@polydopamine (TiO_2@PDA) core–shell composites integrated with polyvinylidene fluoride (PVDF) membranes, which demonstrated enhanced photodegradation efficiency and excellent reusability after ten oxidation cycles.[25] These studies confirm that PDA can serve as an efficient surface modifier to inhibit electron–hole recombination by facilitating charge separation and transfer. Meanwhile, PDA functions as both an electron donor and hole conductor under photoexcitation, thereby enhancing the photocatalytic activity of semiconductor materials.[26,27]

Based on these insights, this study proposes a novel 20D-BOB@PDA monolithic photocatalytic reactor. The BOB@PDA composite catalyst was synthesized *via* a solvothermal process and subsequently loaded on an FDM-printed 20D support. Under LED irradiation (410–420 nm), the effect of PDA introduction on RhB degradation efficiency was systematically evaluated. The research results indicate that PDA can effectively inhibit the recombination of photogenerated electron–hole pairs in BiOBr, thereby significantly enhancing its photocatalytic activity towards organic dye pollutants. Meanwhile, the robust structure and recyclability of the 20D model ensure excellent operational stability and practical applicability. This work provides a feasible and targeted strategy for advancing sustainable environmental remediation using photocatalytic systems.

Materials and methods

Chemical reagents and materials

Bismuth nitrate pentahydrate ($Bi(NO_3)_3 \cdot 5H_2O$), potassium bromide (KBr), anhydrous ethanol, ethylene glycol, and Tris-HCl buffer were purchased from Sinopharm Chemical Reagent Co., Ltd. Dopamine hydrochloride (DA), rhodamine B (RhB), methylene blue (MB), methyl orange (MO), and tetracycline (TC) were obtained from Shanghai Macklin Biochemical Technology Co., Ltd. PLA/PBAT/*Chlorella* 3D printing filaments containing 20 phr of *Chlorella* were self-prepared in the laboratory.[20]

Preparation of the 20D-BOB@PDA catalysts

Initially, the PLA/PBAT/*Chlorella* filament containing 20 phr of *Chlorella* was 3D-printed into a D-type model, referred to as the 20D model. The printed models were placed into an Erlenmeyer flask containing 20 mL of deionized water, subjected to ultrasonic cleaning for 10 min, and subsequently dried in an oven at 80 °C for 12 h. The dried monolithic supports were accurately weighed prior to photocatalyst deposition. To prepare the dopamine solution (solution A), 0.04 g of dopamine hydrochloride was dissolved in 20 mL of Tris-HCl buffer (10 mM, pH = 8.5) and stirred in a constant-temperature shaker at 25 °C and 200 rpm for 24 h. Simultaneously, to prepare the BiOBr precursor solution (solution B), 0.97 g of $Bi(NO_3)_3 \cdot 5H_2O$ and 0.238 g of KBr were dissolved in a mixture of 13.3 mL of anhydrous ethanol and 6.7 mL of ethylene glycol, followed by ultrasonication for 5 min to ensure complete dissolution. Solution A was then added dropwise into solution B under

continuous stirring at 25 °C and 200 rpm for 1 h. The resulting mixture was transferred into a 50 mL Teflon-lined stainless-steel autoclave and subjected to a solvothermal reaction at 120 °C for 8 h. After the system cooled to room temperature, the product was transferred into a 50 mL beaker, and the pretreated 20D model was immersed in the solution. The beaker was shaken at 25 °C and 200 rpm for 1 h to ensure uniform deposition. The 20D model was then retrieved, rinsed thoroughly with deionized water three times, and dried in a vacuum oven at 110 °C for 8 h to obtain the final photocatalyst, denoted as 20D-BOB@PDA. The actual loading amounts of BiOBr and PDA on the 3D-printed monolithic support were quantified by the mass difference method, based on the weight change of the 20D model before and after the photocatalyst deposition. The load amounts of BiOBr and PDA were approximately 1.8% (Table S1).

For comparison, 20D-BOB was prepared following the same procedure but without the addition of solution A (PDA), and BOB and BOB@PDA powder were synthesized following the same solvothermal method without the 20D model (Fig. 1).

Characterization

The surface morphology of the samples was examined using field emission scanning electron microscopy (SEM, SU1510, Hitachi, Japan). The crystal structure was characterized by X-ray diffraction (XRD, D8 Advance, Bruker, Germany). For the XRD analysis, the samples were obtained as isolated powders by carefully separating the photocatalyst from the 3D-printed matrix to minimize background interference and improve diffraction resolution. The elemental composition and chemical states were analyzed using X-ray photoelectron spectroscopy (XPS, Escalab 250xi, Thermo Fisher, USA). All XPS binding energy values were calibrated using the C 1s peak at 284.8 eV and are reported with a uniform precision of one decimal place. The instrumental energy resolution of the XPS system was approximately ±0.1 eV, which was taken into account while evaluating the statistical significance of the binding energy shifts discussed in this work. The optical properties were determined using UV-Vis spectrophotometry (UV-3600, Shimadzu, Japan). The chemical structures of the samples were characterized using Fourier-transform infrared spectroscopy (FT-IR, Nicolet 5700, Thermo Fisher, USA).

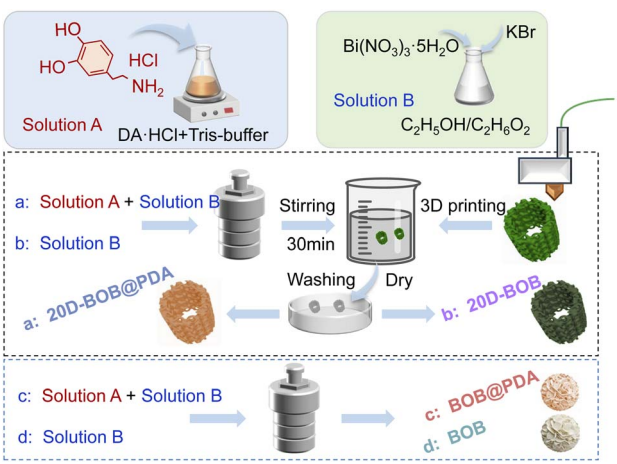

Fig. 1 Schematic of the synthesis process of photocatalysts.

Photocatalytic degradation of RhB

To investigate the influence of the PDA content on the photocatalytic performance, RhB degradation experiments were carried out using the 20D-BOB@PDA catalysts synthesized with varying volumes of dopamine solution (10, 15, 20, 25, and 30 mL). In each experiment, the catalyst was dispersed in 50 mL of an aqueous RhB solution (20 mg L^{-1}). Prior to light irradiation, the suspension was maintained in the dark to establish an adsorption–desorption equilibrium (Fig. S3). During photocatalytic testing, 3 mL aliquots were collected at 30 min intervals, and the residual RhB concentration was quantified by UV-vis spectrophotometry at 554 nm. In addition, the reusability of the photocatalytic system was assessed through at least three consecutive RhB degradation cycles. The results demonstrated good catalytic stability and negligible performance variation (Fig. S4), thereby confirming the reliability of the system for subsequent investigations.

The photocatalytic degradation kinetics were evaluated using the pseudo-first-order model:

$$-\ln(C_t/C_0) = kt \quad (1)$$

where C_0 and C_t represent the initial and instantaneous concentrations of RhB, respectively, and k denotes the apparent first-order rate constant.

To elucidate the dominant reactive species involved in the photocatalytic process, scavenger experiments were performed by introducing specific quenchers: ammonium oxalate (AO) for h^+, potassium dichromate ($K_2Cr_2O_7$) for e^-, benzoquinone (BQ) for $\cdot O_2^-$, and isopropanol (IPA) for ·OH. All experimental conditions were kept identical to those of the RhB degradation experiments, except for the addition of the scavengers.

Results and discussion

Characterizations of 20D-BOB, 20D-PDA and 20D-BOB@PDA

The XRD patterns of the prepared samples are presented in Fig. 2a. Distinct diffraction peaks were observed at 2θ values of 10.9°, 25.2°, 31.7°, 32.2°, 39.4°, 46.2°, and 57.1°, which could be indexed to the (001), (101), (102), (110), (112), (200), and (212) crystal planes of tetragonal BiOBr (JCPDS No. 09-0393), respectively, confirming the successful formation of crystalline BiOBr *via* the solvothermal synthesis process. To further evaluate the effect of PDA incorporation on the crystallinity of BiOBr, the average crystallite sizes of BiOBr before and after PDA modification were estimated using the Scherrer equation based on the full width at half maximum (FWHM) of the (110) crystal planes.[28] Notably, after PDA incorporation, a slight increase in the diffraction peak intensity, accompanied by a marginal decrease in FWHM, was observed, leading to a modest increase in the calculated crystal size (Fig. S5, Table S2).[29] These results indicated that PDA modification did not deteriorate the crystalline structure of BiOBr; instead, it may

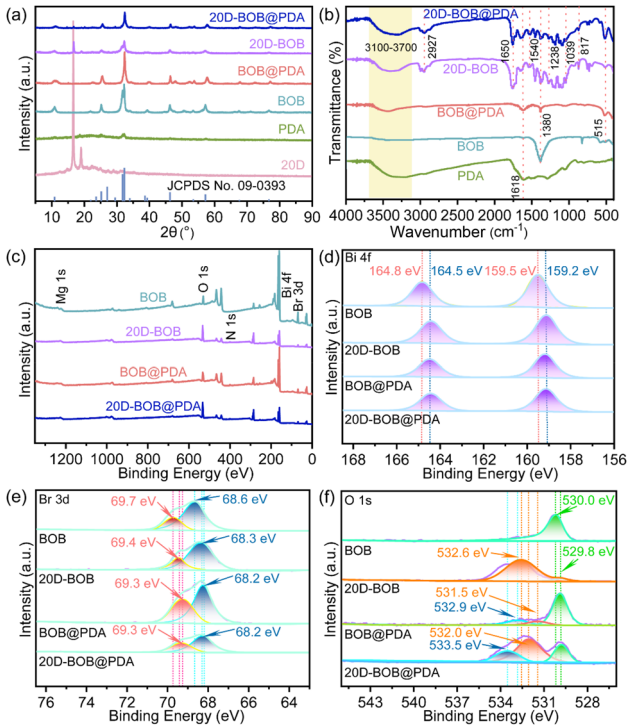

Fig. 2 Characterizations of the as-prepared samples. (a) XRD patterns, (b) FT-IR spectra, (c) XPS survey spectra, and (d) Bi 4f, (e) Br 3d, and (f) O 1s XPS spectra.

have facilitated the improved crystallite growth or lattice ordering, possibly due to interfacial interactions between PDA and BiOBr during the modification process. Moreover, PDA incorporation influenced the relative exposure of BiOBr crystal facets. The diffraction intensity of the (110) plane was enhanced, whereas that of the (102) plane was significantly decreased after PDA modification, suggesting that PDA preferentially interacted with specific facets and subtly modulated the growth orientation of the BiOBr crystals. For the composite samples (20D-BOB and 20D-BOB@PDA), a moderate attenuation of the overall diffraction intensity was observed, which could be attributed to the dilution effect caused by the polymeric PLA/PBAT matrix rather than a reduction in the BiOBr crystallinity. In addition, the weak diffraction peaks appearing in the 2θ range of 15°–20° corresponded to the characteristic diffraction of the PLA/PBAT substrate, further confirming the coexistence of the photocatalyst and polymeric support within the composite system.

FTIR spectroscopy was employed to investigate the surface functional groups of PDA, BOB, BOB@PDA, 20D-BOB, and 20D-BOB@PDA, as shown in Fig. 2b. For pristine PDA, the absorption peak at 1618 cm^{-1} corresponded to the C=C stretching vibration of the aromatic rings of dopamine,[30] while the broad band in the range of 3100–3700 cm^{-1} was assigned to the stretching vibrations of O–H and N–H groups. In BOB, characteristic peaks at 1380 and 515 cm^{-1} were assigned to the Bi–Br and Bi–O stretching vibrations, respectively, confirming the formation of BiOBr. For BOB@PDA, characteristic peaks appeared at 3100–3700, 1618, 1380, and 515 cm^{-1}, corresponding to the O–H and C=C vibrations of PDA and the Bi–Br and Bi–O bonds of BiOBr, respectively, indicating successful surface modification.[31] In 20D-BOB, the bands at 3100–3700, 1655, and 817 cm^{-1} were attributed to the O–H, C=O, and C–O–C stretching vibrations from *Chlorella* in the 20D model, respectively,[20,32] while the Bi–Br and Bi–O stretching vibrations of BiOBr appeared at 1380 and 515 cm^{-1}, respectively. In 20D-BOB@PDA, the broad peak at 3100–3700 cm^{-1} arose from the combined O–H stretching of PDA and *Chlorella*, the peak at 1655 cm^{-1} corresponded to the C=O stretching in *Chlorella*, and the band at 1618 cm^{-1} represented the C=C stretching in PDA. The Bi–Br and Bi–O vibrations of BiOBr were observed at 1380 and 515 cm^{-1}, respectively, while additional bands at 1039 and 817 cm^{-1} were assigned to the C–H and C–O–C vibrations of *Chlorella*. Furthermore, peaks at 2927 cm^{-1} were associated with the CH_3 antisymmetric stretching vibrations of lipids and proteins, 1650 cm^{-1} corresponded to the C=O stretching in proteins, 1540 cm^{-1} to amide N–H bending, and 1238 cm^{-1} to the P=O stretching of phospholipids, DNA, and RNA from *Chlorella*. Notably, upon PDA modification, distinct spectral changes beyond simple peak superposition were observed. For 20D-BOB@PDA, the O–H/N–H stretching band shifted toward lower wavenumbers and became broader compared with that of 2D-BOB (Fig. S6), indicating the formation of strong interfacial hydrogen bonding between the hydroxyl/amine groups of PDA and the surface oxygen or bromine atoms of BiOBr. Such a red shift is commonly associated with strengthened hydrogen-bond interactions rather than mere physical mixing.[33,34]

Raman spectroscopy was further employed to probe possible interfacial interactions between BiOBr and PDA. As shown in Fig. S7, pristine BiOBr exhibits characteristic bands at approximately 61, 110, and 164 cm^{-1}, which are assigned to the external A_{1g}, internal A_{1g} and internal E_{1g} stretching modes of Bi–Br bonds, respectively. These features are consistent with those reported for BiOBr,[35] confirming that its crystal structure remains intact after composite formation. Notably, upon the incorporation of PDA, the BiOBr-related Raman peaks showed a significant decrease in intensity, along with a slight shift to relatively low wavenumbers (Fig. S7). This could be attributed to the surface coverage by the PDA layer and the interfacial interactions between PDA and BiOBr, which may promote interfacial charge transfer during photocatalytic reactions.

The surface composition and chemical state of the prepared samples were investigated using XPS. Detailed analyses were performed for elements Bi, O, Br, C, and N in the BOB, 20D-BOB, BOB@PDA, and 20D-BOB@PDA samples. As shown in the survey spectra (Fig. 2c), the BOB sample primarily contained Bi, O, and Br, which are characteristic of pure BiOBr. In contrast, the other three samples exhibited additional peaks corresponding to C and N, originating from the polymeric 20D model and PDA. Moreover, both 20D-BOB and 20D-BOB@PDA displayed a weak Mg signal derived from the chlorophyll present in *Chlorella* within the 20D model, further confirming the successful incorporation of biological components.

The high-resolution spectra of Bi 4f, Br 3d, and O 1s are shown in Fig. 2d–f. The Bi 4f spectrum of pure BiOBr exhibited

two characteristic peaks at 164.8 eV (Bi $4f_{5/2}$) and 159.5 eV (Bi $4f_{7/2}$),[36] with a spin–orbit splitting of 5.3 eV, indicative of Bi^{3+} in BiOBr. In the spectra of 20D-BOB, BOB@PDA, and 20D-BOB@PDA, the Bi 4f binding energies shifted slightly to low values (164.5 and 159.2 eV), suggesting a reduction of approximately 0.3 eV. This shift was likely attributed to the formation of hydrogen bonds between the O–H groups in *Chlorella* or PDA and the Bi–O framework, as hydrogen bonding interactions typically lower the binding energy of electron-rich atoms.[37,38] Similarly, the Br 3d spectra of BOB showed peaks at 69.7 eV (Br $3d_{3/2}$) and 68.6 eV (Br $3d_{5/2}$)[39] (Fig. 2e). Slight redshifts were observed for 20D-BOB (69.4 and 68.3 eV) and BOB@PDA/20D-BOB@PDA (69.3 and 68.2 eV), which were consistent with the Bi 4f results and further confirmed the electron redistribution induced by interfacial interactions between BiOBr and PDA or the biological matrix.[40] The O 1s spectra provided further insight into the oxygen species in the samples (Fig. 2f). For pure BiOBr, the dominant peak at 530.0 eV corresponded to lattice oxygen in the Bi–O bonds. In 20D-BOB, additional components appeared at 532.6 eV (O–H from *Chlorella*) and 529.8 eV (Bi–O). For BOB@PDA, three distinct peaks were observed at 532.9 eV (C–O in PDA),[24] 531.5 eV (O–H), and 529.8 eV (Bi–O). In 20D-BOB@PDA, the O 1s peaks at 533.5, 532.0, and 529.8 eV corresponded to C–O in PDA, O–H from *Chlorella* and PDA, and Bi–O in BiOBr, respectively.

These results collectively confirmed that BOB@PDA was successfully synthesized and effectively immobilized onto the 3D-printed 20D model. The observed binding energy shifts indicated strong interfacial interactions among BiOBr, PDA, and the *Chlorella*-based polymer matrix, which were beneficial for enhancing charge transfer and photocatalytic performance.

The surface morphologies of 20D-BOB, 20D-PDA, and 20D-BOB@PDA were characterized by SEM to elucidate the structural features and confirm the successful formation of the composite system (Fig. 3). As shown in Fig. 3a and b, the BiOBr in the 20D-BOB sample exhibits regular spherical microstructures composed of closely stacked nanosheets, indicating a well-defined self-assembled hierarchical morphology. In contrast, Fig. 3c and d show that the 20D-PDA sample consists of irregular granular aggregates, which are characteristic of polymerized polydopamine. For the 20D-BOB@PDA composite, granular PDA particles were observed to adhere uniformly to the surfaces of the spherical BiOBr particles, forming a coherent composite interface (Fig. 3e and f). A magnified view (inset of Fig. 3f) further confirmed that BiOBr retained its intrinsic sheet-assembled spherical morphology after the PDA modification, while the PDA nanoparticles were evenly distributed over the surface, indicating successful surface functionalization without disrupting the original particle size and morphology. Quantitative particle size analysis was performed based on the SEM images by measuring the diameters of more than 100 representative particles using image analysis software (Fig. S8). The results showed that the BiOBr spheres possessed an average particle size of approximately 3.52 μm, with a relatively narrow size distribution, suggesting good morphological uniformity.

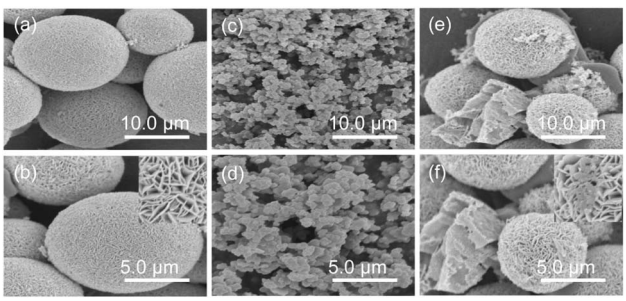

Fig. 3 SEM images of (a and b) 20D-BOB, (c and d) 20D-PDA and (e and f) 20D-BOB@PDA.

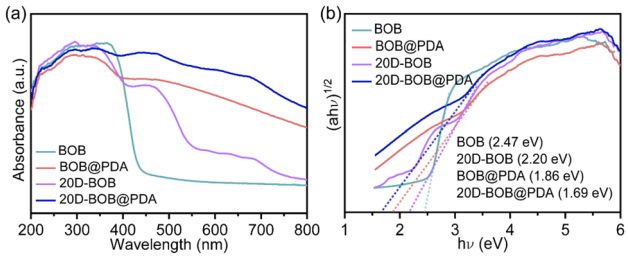

Fig. 4 (a) UV-vis DRS and (b) $(\alpha h\nu)^{1/2}$ *versus* $h\nu$ curves of BOB, BOB@PDA, 20D-BOB and 20D-BOB@PDA.

Optical properties

The optical absorption properties of BOB, BOB@PDA, 20D-BOB, and 20D-BOB@PDA were investigated using UV-vis diffuse reflectance spectroscopy (DRS), as shown in Fig. 4. Compared with pristine BiOBr, all modified samples exhibited markedly enhanced absorption in the visible-light region (400–800 nm) (Fig. 4a). For 20D-BOB, the increased visible-light absorption was primarily attributed to the chlorophyll originating from the *Chlorella* embedded in the 3D-printed 20D model, which acted as a photosensitizer and introduced additional light-harvesting capability without altering the intrinsic electronic band structure of BiOBr. In contrast, the enhanced absorption observed for BOB@PDA mainly arose from the broadband optical absorption of polydopamine, which featured π–π* transitions and tail-state absorption, extending across the visible region. Notably, 20D-BOB@PDA exhibited the strongest and broadest visible-light absorption among all samples. This enhancement was ascribed to the complementary contributions of chlorophyll and PDA: chlorophyll predominantly enhanced absorption in the blue-red regions *via* photosensitization, while PDA provided continuous broadband absorption and facilitated interfacial charge transfer (Fig. S9).[41] Rather than independently narrowing the intrinsic band gap of BiOBr, both components mainly improved visible-light utilization through surface sensitization and light-harvesting effects. The optical band gap (E_g) was estimated using the Kubelka–Munk-transformed Tauc plots according to the following relation:[42]

$$\alpha h\nu = A(h\nu - E_g)^{n/2} \quad (2)$$

where α, h, ν, E_g and A are the absorption coefficient, Planck's constant, optical frequency, bandgap energy, and proportionality

constant, respectively. The value of n is determined by the type of optical transition in the semiconductor.[43] For direct bandgap semiconductors, $n = 1$; for indirect bandgap semiconductors, $n = 4$. BiOBr is an indirect bandgap semiconductor, so its n value is 4. As shown in Fig. 4b, the calculated E_g values follow the order: BOB (2.47 eV) > 20D-BOB (2.20 eV) > BOB@PDA (1.86 eV) > 20D-BOB@PDA (1.69 eV). The reduced bandgap of 20D-BOB@PDA indicated an enhanced ability to absorb visible light and promote photoexcited electron transition, thereby facilitating efficient photocatalytic reactions under visible irradiation.

Notably, the introduction of PDA led to a pronounced decrease in photoluminescence intensity (Fig. S10), indicating that the radiative recombination of photogenerated electron–hole pairs was significantly suppressed. This PL quenching effect could be attributed to the accelerated interfacial charge transfer between PDA and BiOBr, whereby photogenerated electrons and holes were rapidly extracted and consumed in redox reactions rather than undergoing recombination. Although a relatively small bandgap could potentially increase electron–hole recombination, the presence of PDA mitigated this effect by acting as an electron mediator that improved charge separation and transfer efficiency. Consequently, the combination of the 20D model, BOB, and PDA resulted in a composite system with superior visible-light absorption and charge carrier dynamics, accounting for the outstanding photocatalytic performance of 20D-BOB@PDA.

Photocatalytic investigation

To assess the photocatalytic performance of the 20D-BOB@PDA composites prepared with varying PDA contents, RhB was selected as a representative organic pollutant for degradation experiments. As shown in Fig. 5a, the photocatalytic degradation efficiency of 20D-BOB@PDA for RhB exhibited a non-linear trend, initially increasing with PDA content and subsequently declining. Specifically, for dopamine solution additions of 10, 15, 20, 25, and 30 mL, the corresponding RhB degradation efficiencies within 1 h were 47.4%, 55.4%, 95.0%, 65.3%, and 33.6%, respectively. This behavior could be attributed to the dual role of PDA in the photocatalytic process. At moderate concentrations, PDA effectively facilitated electron transfer through its redox-active functional groups and π-conjugated structure, thereby enhancing the separation and migration of photogenerated charge carriers. Consequently, the photocatalytic efficiency of BiOBr was significantly improved. However, excessive PDA loading introduced adverse effects: the thick PDA layer may hinder light absorption by BiOBr and act as an electron-trapping barrier, reducing charge transfer efficiency and leading to a decline in photocatalytic activity.[27] These results demonstrated that PDA modification could substantially enhance the photocatalytic degradation performance of BiOBr, with the optimal activity achieved for the composite prepared using 20 mL of dopamine solution. Therefore, subsequent studies focused on the 20D-BOB@PDA (20 mL) catalyst to further investigate its photocatalytic behavior and mechanism.

The effect of solution pH on the photocatalytic degradation efficiency of 20D-BOB@PDA was investigated. To assess the

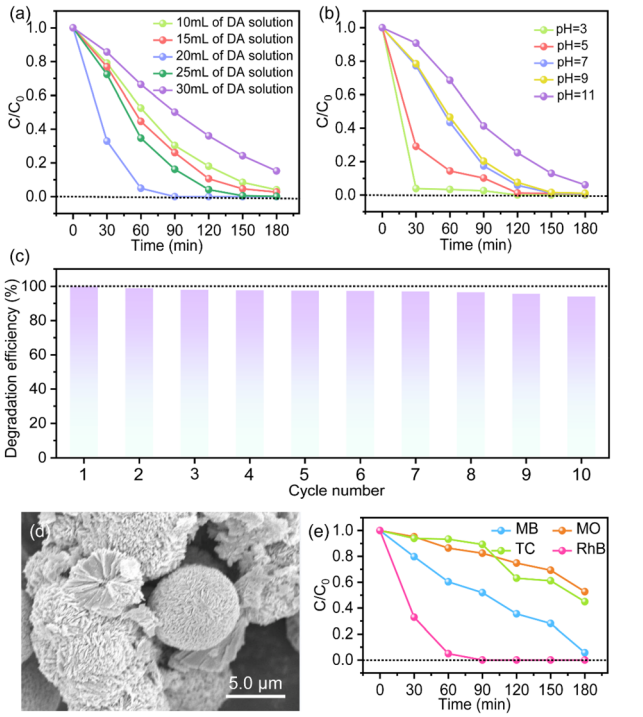

Fig. 5 Photocatalytic degradation curves of 20D-BOB@PDA. Effects of (a) dopamine solution dosages and (b) initial pH on the photocatalytic degradation of 20 mg L^{-1} RhB by 20D-BOB@PDA. (c) Cyclic experiments on the photocatalytic degradation of RhB by 20D-BOB@PDA. (d) SEM image of 20D-BOB@PDA after 10 cycles. (e) Photocatalytic degradation curves of various pollutants (MB, MO, TC, and RhB) using 20D-BOB@PDA.

influence of initial pH, RhB solutions with pH values of 3, 5, 7, 9, and 11 were subjected to photocatalytic degradation experiments. As shown in Fig. 5b, the degradation efficiencies of 20 mg L^{-1} RhB within 1 h were 96.8%, 85.6%, 56.5%, 53.4%, and 31.6%, respectively. Under highly acidic conditions (pH = 3), RhB degradation reached 96.2% within just 30 min, indicating that acidic environments favoured the adsorption of RhB molecules onto the 20D-BOB@PDA surface and promoted subsequent photocatalytic degradation. At pH values of 7, 9, and 11, extended irradiation (2–3 h) allowed degradation rates to reach 94.3%, 92.5%, and 94%, respectively, demonstrating that PDA incorporation enhances pollutant adsorption and mitigates the adverse effects of alkaline conditions. In contrast, unmodified BOB and 20D-BOB exhibited significantly low degradation efficiencies under alkaline conditions.[44] These results indicated that PDA not only improved the overall catalytic activity but also stabilized the performance across a wide pH range, which are advantageous for practical wastewater treatment.

The photocatalytic stability and recyclability of 20D-BOB@PDA were evaluated through RhB degradation cycles. As shown in Fig. 5c and S11, the RhB degradation efficiency of 20D-BOB@PDA remained at 90.0% within 1 h even after 10 continuous cycles, demonstrating excellent cycling stability. The post-reaction structural integrity of the catalyst was further evaluated by SEM and XPS (Fig. 5d and S12). The results showed that the BOB@PDA particles remained uniformly distributed on the 20D

support, retaining their characteristic spherical morphology, as well as the BiOBr and PDA components. No obvious structural deterioration or particle aggregation was observed, confirming the robustness of the composite under repeated photocatalytic conditions. In conclusion, 20D-BOB@PDA exhibited outstanding reusability and structural stability, with negligible loss of photocatalytic activity and morphology even after multiple cycles, highlighting its potential for practical wastewater treatment applications.

The photocatalytic activity of 20D-BOB@PDA for different classes of pollutants was further evaluated using cationic dyes (RhB and MB), an anionic dye (MO), and an antibiotic (TC) at 20 mg L^{-1} (Fig. 5e). The results indicated that RhB was the most efficiently degraded pollutant, achieving 95.0% removal within 1 h and complete degradation within 90 min. In contrast, MB, MO, and TC reached degradation efficiencies of 94.3%, 47.3%, and 55.0% after 3 h, respectively. The higher degradation rate of RhB compared to MB could be rationalized by their electronic structures: the HOMO and LUMO potentials of RhB were 0.95 eV and −1.42 eV (NHE),[45] whereas for MB, they were 1.6 eV and −0.25 eV (NHE).[46] Since the LUMO of RhB was more negative than that of MB and the $O_2/\cdot O_2^-$ redox potential was −0.33 eV, photoexcited electrons from RhB could more readily transfer to the photocatalyst conduction band, facilitating fast degradation.[47] The low degradation efficiency toward anionic MO could be ascribed to electrostatic repulsion between negatively charged MO molecules and the 20D-BOB@PDA surface, resulting in suppressed adsorption and diminished photocatalytic activity. In contrast, the relatively moderate degradation of TC was primarily associated with its intrinsically stable molecular structure, which consisted of a rigid tetracyclic conjugated backbone bearing multiple hydroxyl, carbonyl, and amide functionalities.[48] This polycyclic framework endows TC with high structural robustness and resonance stabilization, while its amphoteric nature and pH-dependent ionization further complicate effective adsorption and reactive site accessibility. As a result, TC is less susceptible to radical-induced ring cleavage and resists efficient decomposition under visible-light irradiation (Fig. S13).

Overall, these findings highlighted that PDA functionalization enhanced both adsorption and charge separation, thereby improving photocatalytic efficiency and reducing the influence of solution pH and pollutant type on the degradation performance.

To elucidate the reactive species involved in the photocatalytic degradation of RhB by 20D-BOB@PDA, selective scavenger experiments were conducted. As shown in Fig. 6a, the RhB degradation efficiency within 1 h decreased from 95.0% (without a scavenger) to 33.9% (BQ), 34.3% ($K_2Cr_2O_7$), 49.7% (IPA), and 52.0% (AO). After 3 h, the degradation efficiencies reached 60.8%, 87.1%, 94.5%, and 95.5%, respectively. These results indicated that $\cdot O_2^-$, e^-, $\cdot OH$, and h^+ all contributed to RhB degradation, with $\cdot O_2^-$ identified as the dominant reactive species, as evidenced by the largest inhibition observed in the presence of BQ. Fig. 6b shows the k-value plots of degraded RhB before and after the addition of the scavengers. All four scavengers inhibited the degradation of RhB to different degrees,

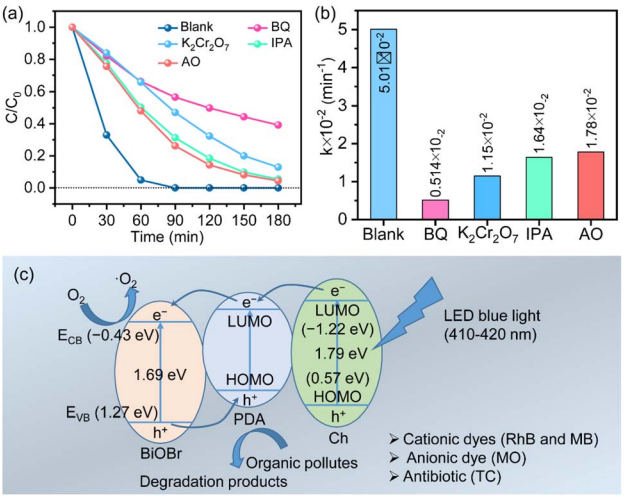

Fig. 6 Effect of different scavengers on (a) RhB degradation efficiency and (b) k-value plots. Photocatalytic self-cleaning mechanism of 20D-BOB@PDA.

but the one that played the most dominant role was $\cdot O_2^-$, which indicated that $\cdot O_2^-$ was the most dominant active substance in the degradation process. A proposed mechanistic pathway for RhB degradation is illustrated in Fig. 6c. Upon visible-light irradiation ($h\nu$), BiOBr acted as the primary photocatalyst, generating electron–hole pairs across its conduction band (CB) and valence band (VB), calculated as follows:[49,50]

$$E_{CB} = \chi - E_e - 0.5E_g \quad (3)$$

$$E_{VB} = \chi - E_e + 0.5E_g \quad (4)$$

where χ is the absolute electronegativity of BiOBr, E_e is the energy of free electrons on the hydrogen scale (~4.5 eV), and E_g is the bandgap (~1.69 eV).[51] E_{CB} and E_{VB} are the conduction band and valence band positions, respectively. The E_{CB} of BiOBr was calculated to be −0.43 eV and E_{VB} to be 1.26 eV. The *Chlorophyll* in the 20D model played a crucial role in absorbing visible photons, promoting electrons from its HOMO (0.57 V *vs.* NHE) to its LUMO (−1.22 V *vs.* NHE) *via* π–π* transitions. Upon light irradiation, PDA was photoexcited to generate electrons in its LUMO and holes in its HOMO. Due to the favorable energy-level alignment and strong interfacial interaction between PDA and BiOBr, the excited electrons were readily transferred from the LUMO of PDA to the CB of BiOBr, together with electrons generated by the direct light absorption of PDA. These electrons accumulated on the CB of BiOBr effectively reduced surface-adsorbed O_2 to produce superoxide radicals ($\cdot O_2^-$). Meanwhile, photogenerated holes in the valence band (VB) of BiOBr were transferred to the HOMO of PDA, resulting in an efficient spatial separation of charge carriers.

Conclusions

The incorporation of PDA effectively suppressed the recombination of photogenerated electron–hole pairs, thereby

enhancing the photocatalytic degradation efficiency of various pollutants, including cationic dyes (RhB and MB), an anionic dye (MO), and an antibiotic (TC). The 20D-BOB@PDA photocatalyst demonstrated the most pronounced degradation toward RhB (95.0% within 1 h), while the degradation efficiencies for MB, MO, and TC reached 94.3%, 47.3%, and 55.0%, respectively, after 3 h. Reactive species trapping experiments identified superoxide radicals ($\cdot O_2^-$) as the predominant reactive species responsible for RhB. Moreover, cyclic stability tests indicated that after 10 continuous cycles, the degradation efficiency of 20D-BOB@PDA for RhB remained at 90% within 1 h, confirming its excellent reusability and stability. Under acidic conditions (pH 3), with an initial RhB concentration of 20 mg L^{-1}, the 20D-BOB@PDA catalyst achieved a remarkable degradation rate of 96.2% within 30 min, demonstrating rapid and high-efficiency photocatalytic activity. In neutral and mildly alkaline conditions (pH 7 and 9), RhB degradation reached 94.3% and 92.5% after 2 h, respectively, indicating that the catalyst maintained strong performance across a broad pH range. Even under strongly alkaline conditions (pH 11), extending the reaction time to 3 h enabled the degradation rate to reach 94%, illustrating that long irradiation could effectively offset the inhibitory effects of high pH and achieve efficient pollutant removal. These results confirmed that 20D-BOB@PDA exhibited excellent photocatalytic activity and stability, making it a promising candidate for practical wastewater treatment applications.

Author contributions

Fengrui Wu: methodology, data curation, writing original draft. Yan Li: methodology, investigation, formal analysis, data curation. Wenxiu Wu: formal analysis, data curation. Zhipeng Zhang: formal analysis. Liangbin Lin: conceptualization. Songwei Yang: formal analysis. Lihong Xu: formal analysis, conceptualization. Xinshu Xia: formal analysis, conceptualization. Weiming Zhou: writing – review & editing, formal analysis, supervision. Changlin Cao: writing – review & editing, resources, funding acquisition, conceptualization. Liren Xiao: writing-review & editing, resources.

Conflicts of interest

There are no conflicts to declare.

Data availability

The authors affirm that the data supporting the findings of this study are included in the article; additional data can be made available from the corresponding author upon reasonable request.

Supplementary information (SI): additional supporting data and characterization results related to this work. It includes digital photographs of the 3D-printed monolithic photoreactor (Fig. S1), photocatalytic degradation and dark adsorption curves (Fig. S2–S4, S13), XRD patterns (Fig. S5), FT-IR and Raman spectra (Fig. S6 and S7), particle size distribution (Fig. S8), UV-vis DRS and Tauc plots (Fig. S9), photoluminescence spectra (Fig. S10), cycling stability tests (Fig. S11), SEM images and XPS spectra of fresh and cycled samples (Fig. S12), as well as tables summarizing the loading capacity of 20D-BOB@PDA (Table S1) and crystal size calculations based on the Scherrer equation (Table S2). See DOI: https://doi.org/10.1039/d6ra01291d.

Acknowledgements

This work is supported by the Fujian Provincial Department of Science and Technology (2025J01661 and 2023L3006) and the Fuzhou Municipal Science and Technology Bureau (2023-ZD-005).

Notes and references

1 G. Wang, S. Lv, Y. Shen, W. Li, L. Lin and Z. Li, *J. Materiomics*, 2024, **10**, 315–338.
2 S. Bosu and N. Rajamohan, *Int. J. Hydrogen Energy*, 2024, **52**, 61–79.
3 S. K. Loeb, P. J. J. Alvarez, J. A. Brame, E. L. Cates, W. Choi, J. Crittenden, D. D. Dionysiou, Q. Li, G. Li-Puma, X. Quan, D. L. Sedlak, T. David Waite, P. Westerhoff and J.-H. Kim, *Environ. Sci. Technol.*, 2018, **53**, 2937–2947.
4 R. Zhang, M. Ma, Q. Zhang, F. Dong and Y. Zhou, *Appl. Catal., B*, 2018, **235**, 17–25.
5 R. Zhang, W. Wan, D. Li, F. Dong and Y. Zhou, *Chin. J. Catal.*, 2017, **38**, 313–320.
6 D. Liu, H. Cai, W. Zhou, D. Lei, C. Cao, X. Xia, L. Xiao, Q. Qian and Q. Chen, *RSC Adv.*, 2024, **14**, 1501–1512.
7 N. Fajrina and M. Tahir, *Chem. Eng. J.*, 2019, **374**, 1076–1095.
8 M. Tahir and B. Tahir, *J. Mater. Sci. Technol.*, 2022, **106**, 195–210.
9 X. Wang and Z.-Y. Yuan, *Smart Mater. Devices*, 2025, **1**, 202528.
10 Y. Shao, S. Wang, B. Ma and S. Chen, *Smart Mater. Devices*, 2026, **2**, 202538.
11 Y. Wu, J. He, W. Huang, W. Chen, X. She, Y. Song, W. Zhu, H. Li and H. Xu, *Sep. Purif. Technol.*, 2023, **327**, 124826.
12 M. Li, W. Lei and W. Yu, *Molecules*, 2024, **29**, 5087.
13 F. Guba, J. Timm, H. T. Duong, A. Pashkova, J. Z. Bloh, R. Marschall and D. Ziegenbalg, *Chem. Eng. J.*, 2025, **520**, 164902.
14 H. Zheng, S. Zhu, L. Chen, L. Wang, H. Zhang, P. Wang, K. Sun, H. Wang and C. Liu, *Polymers*, 2025, **17**, 1601.
15 W. Yu, J. Shi, L. Sun and W. Lei, *Molecules*, 2022, **27**, 7373.
16 P. Roudný and T. Syrový, *J. Manuf. Process.*, 2022, **83**, 667–677.
17 J. Galos, Y. Hu, A. R. Ravindran, R. B. Ladani and A. P. Mouritz, *Composites, Part A*, 2021, **151**, 106661.
18 C. Zhu, H. B. Gemeda, E. B. Duoss and C. M. Spadaccini, *Adv. Mater.*, 2024, **36**, 2314204.
19 A. Cai, A. Guo and Z. Ma, *Materials*, 2017, **10**, 541.
20 X. Xia, Y. Li, Z. Liu, S. Yang, C. Cao, W. Zhou, Q. Chen, L. Xiao and Q. Qian, *Int. J. Biol. Macromol.*, 2024, **271**, 132375.

21 Y. K. Jeong, S. H. Park and J. W. Choi, *ACS Appl. Mater. Interfaces*, 2017, **10**, 7562–7573.
22 C.-T. Chen, C. Chuang, J. Cao, V. Ball, D. Ruch and M. J. Buehler, *Nat. Commun.*, 2014, **5**, 3859.
23 H.-K. Chin, P.-Y. Lin, J. Chen, R. Kirankumar, Z.-H. Wen and S. Hsieh, *Appl. Sci.*, 2021, **11**, 4914.
24 L. Li, L. Chi, H. Zhang, S. Wu, H. Wang, Z. Luo, Y. Li and Y. Li, *Appl. Surf. Sci.*, 2022, **580**, 152168.
25 T. M. H. Le, Y.-N. Wang, C. Li, R. Wang and S. Sairiam, *Chem. Eng. J.*, 2024, **499**, 156215.
26 M. d'Ischia, A. Napolitano, V. Ball, C.-T. Chen and M. J. Buehler, *Acc. Chem. Res.*, 2014, **47**, 3541–3550.
27 D. Aguilar-Ferrer, J. Szewczyk and E. Coy, *Catal. Today*, 2022, **397–399**, 316–349.
28 M. Irfan, R. Saleem, B. Shoukat, H. Hussain, S. Shukrullah, M. Y. Naz, S. Rahman, A. A. J. Ghanim, G. Nawalany and T. Jakubowski, *Sci. Rep.*, 2023, **13**, 9057.
29 J. Oh, S. B. Park, C. Cha, D. K. Hwang, S.-A. Park, J. Park, D. X. Oh, H. Jeon and J. M. Koo, *Chemosphere*, 2024, **354**, 141729.
30 L. Yang, C. Chen, Y. Hu, F. Wei, J. Cui, Y. Zhao, X. Xu, X. Chen and D. Sun, *J. Colloid Interface Sci.*, 2020, **562**, 21–28.
31 S. Li, Q. Ma, L. Chen, Z. Yang, M. Aqeel Kamran and B. Chen, *Chem. Eng. J.*, 2022, **433**, 134492.
32 L. S. Ferreira, M. S. Rodrigues, J. C. M. de Carvalho, A. Lodi, E. Finocchio, P. Perego and A. Converti, *Chem. Eng. J.*, 2011, **173**, 326–333.
33 V. L. Furer, A. E. Vandyukov, S. R. Zaripov, S. E. Solovieva, I. S. Antipin and V. I. Kovalenko, *Vib. Spectrosc.*, 2018, **95**, 38–43.
34 M. Du, Y. Du, Y. Feng, K. Yang, X. Lv, N. Jiang and Y. Liu, *Carbohydr. Polym.*, 2018, **195**, 393.
35 A. Phuruangrat, S. Thongtem and T. Thongtem, *J. Electron. Mater.*, 2019, **48**, 8031–8038.
36 Z. Wei, Y. Wang, Z. Shao, L. Xie, L. Zhang, K. Xu and X. Chai, *Molecules*, 2025, **30**, 1735.
37 H. Li, S. Chen, H. Shang, X. Wang, Z. Yang, Z. Ai and L. Zhang, *Sci. Bull.*, 2020, **65**, 1916–1923.
38 W. Fu, J. Wan, H. Zhang, J. Li, W. Chen, Y. Li, Z. Guo and Y. Wang, *Nat. Commun.*, 2022, **13**, 5496.
39 R. Zhang, S. Sun, Z. Hao, L. Wang, Y. Gao and Z.-G. Han, *Appl. Surf. Sci.*, 2026, **716**, 164669.
40 J. Feng, X. Ran, L. Wang, B. Xiao, J. Zhu, Z. Liu, C. Li, R. Li, G. Feng and K. Xu, *Molecules*, 2025, **30**, 538.
41 X. Zhou, B. Jin, J. Luo, X. Xu, L. Zhang, J. Li and H. Guan, *RSC Adv.*, 2016, **6**, 64446–64449.
42 X. Liu, Y. Zhu, S. Gao and Y. Ren, *Appl. Phys. A*, 2024, **130**, 706.
43 C.-J. Chang, Y.-C. Kao, J.-K. Chen, H.-C. Zhang and S.-Y. Wu, *J. Ind. Eng. Chem.*, 2023, **124**, 412–421.
44 Y. Li, L. Lin, F. Wu, L. Xu, Y. Zhang, X. Xia, C. Cao, W. Zhou, L. Xiao, Q. Qian and Q. Chen, *RSC Adv.*, 2025, **15**, 4820–4828.
45 X. Yan, Y. Wang, B. Kang, Z. Li and Y. Niu, *Crystals*, 2021, **11**, 1373.
46 K. Phumivanichakit, S. Suwanboon and P. Amornpitoksuk, *Inorg. Chem. Commun.*, 2023, **156**, 111237.
47 S. Demarema, M. Nasr, S. Ookawara and A. Abdelhaleem, *J. Clean. Prod.*, 2024, **463**, 142679.
48 V. Vinesh, M. Ashokkumar and B. Neppolian, *Ultrason. Sonochem.*, 2020, **68**, 105218.
49 J. C. Pantoja-Espinoza, G. A. DelaCruz-Alderete and F. Paraguay-Delgado, *Catalysts*, 2025, **15**, 851.
50 P. Zhou, I. A. Navid, Y. Ma, Y. Xiao, P. Wang, Z. Ye, B. Zhou, K. Sun and Z. Mi, *Nature*, 2023, **613**, 66–70.
51 Q. Fan, X. Chen, F. Chen, J. Tian, C. Yu and C. Liao, *Appl. Surf. Sci.*, 2019, **481**, 564–575.